LIRAD Observations of Tropical Cirrus Clouds in MCTEX. Part I: Optical Properties and Detection of Small Particles in Cold Cirrus*

C. M. R. PLATT,* S. A. YOUNG,+ R. T. AUSTIN,* G. R. PATTERSON,+ D. L. MITCHELL,# AND S. D. MILLER@

*Department of Atmospheric Science, Colorado State University, Fort Collins, Colorado, and CSIRO Atmospheric Research, Aspendale, Victoria, Australia
+CSIRO Atmospheric Research, Aspendale, Victoria, Australia
#Desert Research Institute, Reno, Nevada
@Naval Research Laboratory, Monterey, California

(Manuscript received 28 March 2000, in final form 11 March 2002)

ABSTRACT

This paper presents further results on the optical properties of tropical and equatorial cirrus using the light detecting and ranging (lidar) radiometer (LIRAD) method. The results were obtained from observations in the Maritime Continent Thunderstorm Experiment (MCTEX). Values were obtained of cirrus cloud backscatter coefficient, infrared (IR) emittance, optical depth and absorption coefficient, cloud height and depth, and backscatter-to-extinction ratio. The values agree well with previous results obtained on equatorial cirrus in the Pilot Radiation Observation Experiment (PROBE) and extend those results to lower temperatures. Observations made of lidar linear depolarization ratio show similar trends to those observed in PROBE, extending those results to lower temperatures.

Regressions of cloud IR emittance and absorption coefficients are performed as a preliminary tropical dataset for both cloud-resolving and climate models. These regressions are compared with previous regressions on midlatitude and tropical synoptic cirrus clouds. The IR absorption coefficients in tropical and equatorial cirrus appear to be larger than in midlatitude cirrus for temperatures less than $-40°C$, with the difference increasing toward low temperatures. Thus, a significantly different relationship may be appropriate for tropical cirrus compared to midlatitude cirrus clouds.

Effective diameters of small particles in the colder tropical clouds are also measured using the ratio of visible extinction to infrared absorption. A new treatment of multiple scattering is used to correct the ratios. Effective diameters range from 6 to 9.3 μm at the colder temperatures.

1. Introduction

This paper describes light detecting and ranging (lidar) radiometer (LIRAD) method results obtained in a tropical region of northern Australia during a period of transition between the dry season and the monsoon season. The results were obtained as part of the Maritime Continent Thunderstorm Experiment (MCTEX), which was held on the Tiwi Islands, about 120 km north of Darwin, Northern Territory, Australia. MCTEX was initiated and planned by the Australian Bureau of Meteorology with collaboration from other Australian and U.S. laboratories. The U.S. Department of Energy Atmospheric Radiation Measurement (ARM) program supported a component of the Commonwealth Scientific and Industrial Research Organization (CSIRO) Atmospheric Research (CAR) study. The experiment also included various radars provided by the U.S. National Oceanographic and Atmospheric Administration (NOAA) and the University of Massachusetts, together with an ARM microwave radiometer. These components were also supported by ARM. The radars and microwave radiometer were sited close to the CSIRO lidar and infrared (IR) radiometer, providing a powerful system for studying cloud structural, optical, and microphysical properties.

The basic scientific objective of MCTEX was to improve knowledge of the dynamics and interaction of the physical processes controlling convection over the Maritime Continent. One ''component scientific objective'' was to document the radiative properties of convectively generated cirrus (Keenan et al. 1994). Such properties have been examined in the present study, with observations here on long-lasting cirrus layers, often observed just below the tropopause. Some of the layers

* Supplemental information related to this paper is available at the Journals Online Web site: http://dx.doi.org/10.1175/JAS2843supl1.

Corresponding author address: Dr. R. T. Austin, Department of Atmospheric Science, Colorado State University, Fort Collins, CO 80523-1371.
E-mail: austin@atmos.colostate.edu

appeared to be associated with extensive cirrus, possibly from distant disturbances, whereas others appeared to be associated with storm anvils that had formed locally over the islands and had largely dissipated. Sekelsky et al. (1999) have reported on millimeter radar studies of the deeper, more attenuating convective storms. Broader reasons for studying cirrus in the climate context have been discussed extensively (by Platt 1997; Platt et al. 1998, hereafter P98; and Stephens et al. 1990, among others). Gates et al. (1999) show results from a collection of different atmospheric general circulation models that demonstrate the large uncertainties that still exist in the prediction of the generation and evolution of clouds.

The aim of the present study was to retrieve the optical properties of tropical cirrus in MCTEX and to use the mean data, together with data from previous tropical and midlatitude studies (Platt et al. 1987; Young et al. 2000), to obtain relations between temperature and various optical quantities. Some regressions of infrared emittance and absorption coefficient in terms of temperature are also formulated and compared with the earlier relation of Platt and Harshvardhan (1988). The regressions obtained can be used as preliminary model input or validation data until more comprehensive global datasets are available.

This paper further presents new results on the retrieval of an effective particle radius from the quantity α, the ratio of the visible extinction coefficient at the lidar wavelength (532 nm in the present study) to the infrared absorption coefficient at the radiometer wavelength (10.86 ± 0.25 μm). Past experimental studies (e.g., Platt et al. 1987; P98) indicated an increase in α with decreasing temperature, particularly at temperatures below -60°C, and similar trends were found in the present study. Original theoretical studies reported by Platt (1979) indicated that for spherical or cylindrical ice particles, α increased significantly for radii less than 10 μm. Recently, an ice-cloud–radiation scheme devised by Mitchell et al. (1996), treating various ice-crystal shapes, has become available and was used in Mitchell and Platt (1999) to account for the P98 results. A bimodal cirrus particle size distribution was used. This scheme showed values of α that again increased with decreasing effective radius and accounted qualitatively for the high values of α found by P98 in PROBE. In the present study, the new ice-cloud–radiation scheme was expanded to incorporate the scattering processes described in Mitchell (2000) and was used to account for the high values of α that were again found at the lowest temperatures in MCTEX.

2. Instrumentation and observations

Observations were made at a site at the Pirlangimpi Golf Club (11.40°S, 130.41°E), Pularumpi, Melville Island, in northern Australia. The CSIRO instruments were operational from 18 November to 8 December 1995. The CSIRO trailer containing the lidar and radiometer was placed next to a two-frequency (33 and 94 GHz) millimeter radar from the University of Massachusetts (Sekelsky and McIntosh 1996), a 3-GHz (S-band) profiler and 915-MHz profiler from the NOAA Aeronomy Laboratory, and a microwave water vapor and liquid water radiometer from the ARM program (Liljegren 1994). In this particular study, the microwave radiometer data were utilized along with data from the CSIRO lidar and infrared radiometer in the LIRAD analysis. Some comparative observations with the radar instrumentation are described in Part II of this series (Platt et al. 2002, hereafter Part II).

TABLE 1. Lidar and radiometer characteristics.

Characteristic	Lidar	Radiometer
Wavelength employed	532 nm	10.86 ± 0.25 μm bandpass
Field of view	2 mrad	8 mrad
Pulse energy, length	160 mJ, 8 ns	
Minimum detectable radiance*		3.67×10^{-3} W m^{-2} sr^{-1} Hz$^{-1/2}$
Detectors	Thorn EMI 9816B photomultipliers with two-channel, 10-bit, 2048-word digitizer	HgCdTe, liquid nitrogen cooled

* 1-s time constant.

a. CSIRO lidar

The CSIRO lidar used during the experiment was a recently completed multiwavelength scanning lidar comprising a QuantaRay CGR 11/3 pulsed, Nd:YAG laser as the transmitter and a 350-mm-diameter, modified Cassegrain telescope as the receiver. Observations during MCTEX were confined to the second harmonic (532 nm), as this gave the best combination of good signal-to-noise ratio and discrimination of clouds and aerosol signals against the molecular backscatter signal. Other equipment parameters are summarized in Table 1.

For most of the experiment, the lidar recorded the total, second harmonic, backscatter signal. During some periods, the dichroic beam-splitter cube was replaced by a polarizing beam splitter that directed the orthogonal polarization components of the 532-nm backscatter signal to separate photomultipliers whose outputs were recorded simultaneously on a two-channel digitizer.

In order to further improve the signal-to-noise ratio in the signals recorded from the very high clouds encountered during MCTEX, the laser was fired at 10 Hz in bursts of up to 256 shots, and the signals were averaged in the digitizer. This procedure was repeated every minute or 30 seconds.

b. CSIRO/ARM radiometer

The new CSIRO/ARM sensitive, narrow-beam, three-channel radiometer (Platt et al. 1993) was operated at

TABLE 2. Mean values of cloud properties for each run.

Date (1995)	No. of profiles	Time (LT)*	Mean base height (km)	Mean cloud depth (km)	Mean midcloud temperature (°C)	Mean emittance
19 Nov	58	1806–1840	13.80	2.32	−72.5	0.013
19 Nov	86	2117–2208	14.68	1.56	−76.3	0.057
20 Nov	32	1003–1045	13.44	2.12	−69.0	0.052
20 Nov	73	1419–1621	13.35	2.29	−68.9	0.130
21 Nov	17	1013–1045	13.92	1.40	−70.0	0.144
21 Nov	39	1348–1457	14.68	0.39	−71.9	0.147
24 Nov	91	1746–1923	14.92	1.96	−79.0	0.122
25 Nov	42	0955–1102	13.44	2.31	−69.9	0.143
25 Nov	160	1510–1833	13.20	2.58	−68.4	0.249
26 Nov	61	1038–1150	13.51	2.82	−71.8	0.087
26 Nov	228	1753–2201	14.10	2.59	−76.0	0.207
29 Nov	45	0943–1130	12.21	2.99	−62.3	0.394
29 Nov	79	2108–2231	12.49	4.92	−73.5	0.317
01 Dec	57	1102–1205	14.25	2.68	−78.0	0.499
01 Dec	49	1554–1650	11.43	2.71	−54.7	0.963
02 Dec	45	0856–1108	10.14	3.52	−47.5	0.080
04 Dec	308	0532–1224	12.86	3.55	−70.6	0.450
04 Dec	48	2206–2304	13.28	4.17	−76.3	0.201
05 Dec	99	0958–1155	9.67	4.96	−49.7	0.293

* LT = UTC + 9 h, 30 min.

10.86 ± 0.25 μm bandpass. Further radiometer characteristics are shown in Table 1. The lidar and radiometer axes were aligned in the vertical, some 2 m apart to observe similar volumes of cloud.

c. Observations

Observations were made every day from 18 November to 8 December, and a total of 132 h of lidar and radiometer data were obtained. Observations were curtailed on most days by periods of lower cumulus clouds and sometimes by rain, but some longer episodes of data were obtained, mainly late in the evenings, when convection had died down, and again in the early morning hours.

A wide range of cirrus-type clouds was observed. Cirrus was sometimes observed quite separate from convective storms, the cirrus having the typical appearance of either cirrus uncinus or cirrus spissatus. At other times, extensive thin layers were observed near the tropopause; these layers appeared to be leftover fragments of storm anvils. The layers had little indication of the fallout patterns that are commonly observed in lower, warmer cirrus, but could, however, assume quite considerable depths and often contained evidence of gravity waves. Mean properties of the clouds included in the present LIRAD study of cirrus (a subset of the MCTEX dataset) are shown in Table 2, indicating the wide ranges in height, depth, and infrared emittance. The cirrus layers just below the tropopause were seldom detected by millimeter radar.

The frequency of radiosonde ascents was dependent on whether an intensive operational period (IOP) was in force. For the LIRAD periods analyzed, the intervals between radiosonde ascents varied between about two and eight hours.

d. Calibration of the lidar and radiometer

The lidar signals were calibrated following essentially the same procedure as that adopted in P98. In this method (Young 1995), the signal, after correction for variable equipment parameters, is fitted using linear regression to a reference signal calculated from a radiosonde-derived density profile. The reference signal is that signal that would be expected from a purely molecular atmosphere (i.e., one that is free of clouds and aerosols). Because the radiosonde profiles rarely extended far above the tropopause, and because the clouds being studied were close to this altitude, the lidar signal was fitted to the reference signal solely in a region below the clouds. To maximize the accuracy of the calibration, this region was typically 2.5–4 km deep, and examined beforehand to ensure that the region had minimal aerosol loading. The calibration thus produced profiles of attenuated backscatter coefficient used in the LIRAD analysis described below. The calculation of the effective optical thickness of the clouds as described by Young (1995) was usually not feasible in this dataset, due to the weak signal from the atmosphere above the clouds and the shallowness of the region above cloud top measured by the radiosondes.

The CSIRO/ARM radiometer utilized a two-point temperature calibration, an improvement on the method used in P98. The radiometer was calibrated at about hourly intervals successively against a blackbody at liquid nitrogen temperature and against a stirred ice–water mixture. The dwell time on each calibration blackbody was 30 s. As shown in appendix A, this procedure removed problems associated with a nonzero signal at the temperature of the reference blackbody (P98). The two-point calibration also reduced any ambient emission effects of the scanning mirror. Previous experiments had

indicated that the output signal was linear with input radiance.

3. Theory and analysis

The theory of the LIRAD method and its applications to tropical cirrus in the ARM Pilot Radiation Observation Experiment (PROBE) are described in P98. The reader is directed to that paper for details of the algorithm; differences unique to the present study and additional comments are given in this section.

a. Definitions and equations

The basic equations for backscatter, emittance, and depolarization ratio are identical to those in section 3 of P98. The multiple scattering used in the theory and analysis is defined by the factor $\overline{\eta}$, the multiple scattering factor for the total cloud depth. It is assumed that multiple scattering between (air) molecules and between aerosols in the cloud is negligible, and that photons scattered by cloud particles and then molecules or aerosols undergo the same multiple scattering as between cloud particles alone (see section 3d). Given that the ratio of cloud particle scattering to molecular or aerosol scattering is usually about 10 or greater, these assumptions are considered to be reasonable. However, because the clouds were often several kilometers deep, the molecular backscatter signals above and below the clouds were significantly different and the molecular attenuation over the cloud depth appreciable, so these effects needed to be considered (Young 1995).

The equations for infrared radiance are again the same as those in section 3 of P98. In order to calculate the radiance, L_c, at cloud base, the radiance at the ground must be corrected for strong water vapor absorption and emission and for other minor components such as CO_2 and aerosols. For cirrus, we make the approximation that all the atmospheric (noncloud) absorption and emission occurs below cloud base. In calculating the absorption radiance L_a, the reflected upwelling radiance L_r is particularly important in tropical atmospheres, where the ground is warm and a small reflection from a very cold cloud can lead to an appreciable fraction of the total emitted radiance. This in turn can lead to ''super-black'' clouds, as found by Platt et al. (1987). Platt and Stephens (1980) calculated theoretically representative scattering and reflection components in tropical cirrus.

Water vapor absorption and emission in the tropical atmosphere were treated in detail by Platt et al. (1984) and P98. The dominant water vapor absorption continuum was treated by Lee (1973) as dimer absorption, and more recently by Clough et al. (1989) as absorption in the wings of strong lines. A dimer absorption coefficient of $9.0 \pm 0.5\ g^{-1}\ cm^2\ atm^{-1}$ was determined as the mean from clear sky observations in P98, a value close to those determined by other workers. A weaker water vapor line spectrum is also included.

The LIRAD method effectively uses the retrieved cloud backscatter coefficient profile $B_c(\pi, z)$ to determine the distribution of the IR absorption coefficient $\sigma_a(z)$ in the cloud column. The ratio between these quantities is assumed to be constant within the cloud and is varied until the measured absorption radiance L_a is equal to a theoretical value L_{at} calculated by a standard radiative transfer equation [(12) in P98]. The IR optical depth, visible optical depth (after correction for multiple scatter), and IR emittance may then be obtained.

The cloud backscatter coefficient $B_c(\pi, z)$ is retrieved from the measured total backscatter using P98's (16)–(18) iteratively from cloud base to cloud top. This requires a value of $k/(2\overline{\eta})$, which is obtained numerically from the value of the integral of the attenuated backscatter coefficient when the emittance tends to unity [see (7) in P98]. At the first iteration, an approximate value of the cloud extinction coefficient $\sigma_c(z)$ is obtained using (19) of P98. The iteration is continued until the change in B_c is less than a small percentage of its value, and the entire process progresses upward through successive altitudes until the cloud top is attained. Molecular (air) backscatter and extinction values in MCTEX were obtained by interpolation from radiosonde profiles of altitude, temperature, and pressure. A radiosonde was launched from a site 10 km distant and at periods varying from 2 to 6 h.

If the cloud optical depth becomes large during the retrieval process, successive values of $B_c(\pi, z)$ can diverge and the retrieval becomes unstable. For those cases, the quantity $k/(2\overline{\eta})$ was increased by a small fraction and the retrieval repeated again from cloud base until values of $B_c(\pi, z)$ could be calculated to cloud top. This process enabled retrieval to cloud top in cases of quite high optical depth. When complete attenuation occurred below cloud top, the retrieval was terminated at that point, but values of $B_c(\pi, z)$ could still be achieved below the effective cloud top. This procedure was used, for instance, in the cases of the very attenuating anvil clouds that are considered in Part II.

b. Correction for noncloud atmospheric absorption and emission

Water vapor absorption and emission in the tropical atmosphere are strong in the atmospheric window. Thus, the cloud radiance at the ground is often only 30%–40% of the true cloud radiance. At the same time, the water vapor radiance can constitute about 10 times the cloud radiance at the ground (P98). Further, the water vapor emission is found to vary in the short term during observation episodes by amounts equal to or greater than the cloud signal. Figure 1 shows an example of the measured atmospheric radiance L_s and the water vapor path during one episode in the present experiment. It is apparent that some of the variations in radiance are cor-

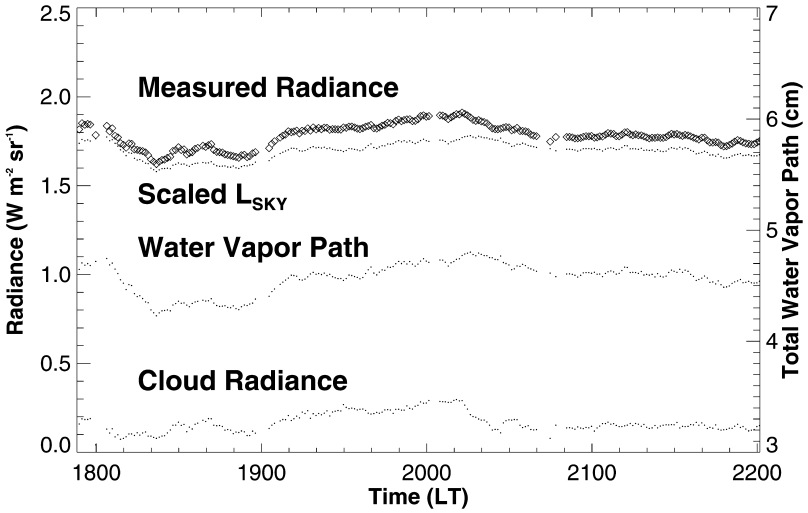

FIG. 1. Measured radiance L_s, scaled water vapor radiance L_{sky}, measured water vapor path, and retrieved cloud radiance L_c, during a measurement period on 26 Nov 1995.

related with variations in water vapor path, as measured by the ARM microwave radiometer. It is thus imperative to make a careful correction for water vapor. Fortunately, the ARM microwave radiometer made a continuous measurement of water vapor path. These data were used to remove the atmospheric below-cloud transmittance and radiance (τ and L_{sky}) on a continuous basis. Using radiosonde data at the times of the launches, a calculated value of L_{sky} is normalized to the calculated water path. The value of L_{sky} at intermediate times can then be obtained from the measured water path using an interpolated normalization factor. This takes into account the height distribution of water vapor at the times of the radiosonde launches. However, such changes occurring between launches are missed, causing further uncertainties. Values of L_{sky} and τ were also calculated with a clear-atmosphere radiative transfer code for all radiosonde profiles and for a range of continuum absorption coefficients. As in P98, this yielded a tight relationship between L_{sky} and τ, indicating that the effects of changes in the atmospheric temperature profile appeared to be secondary to changes in water vapor in the water vapor emission. The data were fitted to an equation of the form

$$\tau = 1.0 - 0.297L_{sky} + 0.00359L_{sky}^2, \qquad (1)$$

which is quite similar to that used in PROBE. Values of τ could then be calculated for each measured value of L_{sky}, and L_c could be calculated from (14) of P98. The scaled radiance L_{sky} and the calculated cloud radiance L_c are shown in Fig. 1, together with the measured radiance and water vapor path. The cloud radiance is seen to be about 15% of the total radiance at maximum, but all the variable water vapor effects have been removed.

Finally, values of integrated attenuated cloud backscatter $\gamma'(\pi)$ are plotted against retrieved cloud radiance L_c. Final adjustments to the value of L_{sky} are then made by varying the water vapor continuum absorption coefficient until values of L_c were zero when (possibly extrapolated) values of $\gamma'(\pi)$ were zero.

A mean continuum absorption coefficient of 9.81 $\pm$ 1.29 g^{-1} cm^2 atm^{-1} was determined for the present experiment. This agreed within the margin of error with the value of 9.0 $\pm$ 0.5 g^{-1} cm^2 atm^{-1} found in P98. The reason for the larger scatter in the present observations is not understood, but it is probably due to large variations in water path with time on certain occasions.

c. Retrieval of cloud particle effective radius

Platt (1979) and Mitchell and Platt (1999) showed how the ratio α is sensitive to effective cloud particle diameter D_e for particles smaller than a few tens of microns (Fig. 2). Thus, this gives us a method for determining D_e in cold tropical cirrus, which is known to contain small particles (see later sections). Mitchell and Platt (1999) used a modified form of the scheme developed by Mitchell et al. (1996) that included bimodal size spectra and photon tunneling processes (Mitchell 2000) to calculate effective diameter in terms of α. This new scheme yields extinction and absorption coefficients within about 10% of Mie theory values for ice spheres for any wavelength and size distribution having an effective radius greater than or equal to 5.0 μm. A key advantage of using this modified anomalous diffraction approximation (ADA) is that it can treat any particle shape, given its projected area- and mass-dimensional relationship. In this work, the contribution from photon tunneling was assumed to be zero, due to recent studies that compared retrieved cirrus particle size at thermal wavelengths with measured in situ particle sizes (Baran et al. 2001;

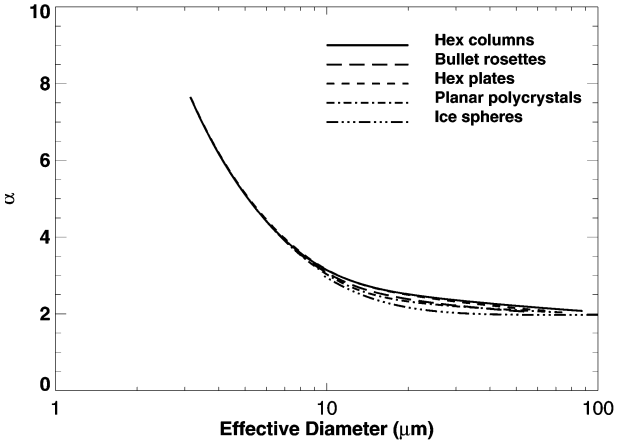

FIG. 2. Theoretical values of α as a function of effective diameter D_e for several ice-crystal habits (after Mitchell et al. 1996).

Francis et al. 1999). These studies, as well as laboratory (Mitchell et al. 1999) and theoretical work using oblate spheroids (Baran et al. 2001) indicate that photon tunneling effects in natural ice crystals tend to be small or negligible. As shown in Mitchell and Platt (1999), α is relatively insensitive to tunneling effects, because these effects largely cancel when taking ratios. Including tunneling produces slightly lower values of α.

Mitchell and Platt (1999) used this modified ADA to make a preliminary investigation of the high values of α found in P98 and to see if such values of α were possible and realistic within known theoretical frameworks. They found that a value of α as high as 4 or 5 was indeed possible for the sorts of size spectra found in cold cirrus clouds. This occurred due to the small ice-crystal photon path relative to a sphere having the same maximum dimension. When the size distribution contains a strong bimodal peak for small crystals less than about 60 μm, the mean photon path for the entire distribution is sufficiently small so that considerable thermal radiation generally penetrates the ice crystals, resulting in absorption efficiencies Q_{abs} considerably less than unity. This results in ratios of visible extinction efficiency Q_{ext} to thermal Q_{abs} considerably greater than 2.

A plot of α versus an effective diameter D_e is shown in Fig. 2. The effective diameter is defined here as

$$D_e = \frac{3}{2}\frac{\text{IWC}}{\Delta_{\text{ice}} P_t}, \tag{2}$$

where IWC is the ice water content, Δ_{ice} is the density of bulk ice, and P_t is the total projected area of the size distribution. This definition of D_e treats extinction and absorption processes with almost the same accuracy as the more explicit treatment of Mitchell et al. (1996) and Mitchell (2000) when using D_e as described in Mitchell et al. (1999). The factor of 3/2 in (2) defines D_e in terms of a sphere having the same effective photon path for a given size distribution.

The calculations show differences in α for various crystal habits commonly found in cirrus. For crystal diameters less than about 9 μm, the curves coincide, but at higher particle sizes, there is some spread in the values of α. This introduces some ambiguity when the cloud particle crystal habit is not well defined. This is discussed further in section 5.

d. Correction for multiple scattering effects

The multiple scattering factor $\overline{\eta}$ is required in order to calculate final values of both k and α. Platt (1981) made a fairly comprehensive study of multiple scattering in cirrus clouds. This study indicated in a systematic manner how the multiple scattering factor varied with telescope field aperture, range, optical depth, and penetration into the cloud, for selected scattering phase functions. Values were found to be extremely dependent on the phase function utilized, particularly near the forward and back directions. Very few other studies on cirrus are available for comparison. The studies reported by Bissonette et al. (1995) for a standard Deirmendjian water cloud indicated the large variability between different codes, even for such a standard water cloud, range, and telescope aperture.

Based on the Platt (1981) data, an approximate relation linking the multiple scattering factor $\overline{\eta}$ to the cloud altitude was formulated in P98. This version was estimated to give $\overline{\eta}$ to an accuracy of about $\pm 25\%$. Because the relation between altitude and temperature in the Tropics is fairly constant, the $\overline{\eta}$ relation was formulated in terms of temperature rather than height. This relation is probably satisfactory for large-particle cirrus typically found at heights up to 10 km. However, for higher cirrus (where larger values of $\alpha\overline{\eta}$ were measured in the P98 data), the above-mentioned relation had to be extrapolated. Now, it was apparent from the PROBE data (P98) that $\alpha\overline{\eta}$ tended to become larger, indicating that particles tended to become progressively smaller at altitudes above 10 km, indicating in turn that scattering phase functions and thus values of $\overline{\eta}$ would also change, and in fact become larger. Thus, the relation used in P98 would become progressively less accurate above 10 km, and a better model was required for the present work.

Information on particle size distributions and equivalent scattering phase functions for low-temperature tropical cirrus is scarce. Schmitt et al. (2000) determined a peak in the maximum particle dimension of 20 μm from observations in tropical cirrus at -54°C. Knollenberg et al. (1993) observed size distributions near the tops of tropical mesoscale convective systems with effective sizes of about 10 μm. Rinsland et al. (1998) determined a particle diameter of 12 μm for tropical clouds between 13- and 16-km altitude. Baran et al. (2001) used a modified Henyey–Greenstein function to mimic observed cirrus phase functions. Such a phase function corresponding to an effective particle diameter

TABLE 3. Values of multiple scattering factor $\overline{\eta}$ for different ranges and particle sizes.

Height (km)	MCTEX temperature (°C)	$\overline{\eta}$ Platt (1981) (large particles)	$\overline{\eta}$ Baran et al. (2001) (small particles)
5	−7	0.48	—
10	−32	0.43	0.72
15	−62	0.41	0.69
20	~−80	0.40	0.68

of 11 μm was supplied (A. Baran 2000, personal communication) for the purposes of calculating a value of $\overline{\eta}$ for the present study. Results, together with those from Platt (1981), are shown in Table 3. The change in $\overline{\eta}$ with temperature is a function of range. In reality, $\overline{\eta}$ would be expected to vary slowly with range; however, only the one value of $\overline{\eta}$ equal to 0.6 ± 0.1 and corresponding to the above particle diameter was used in the present study for the lower temperature ranges, as described later in section 5b.

4. Results from two case studies

We examine two different but representative MCTEX cases: a typical ''cold'' cirrus layer near the tropopause, and more synoptic-type, warmer cirrus clouds at a lower elevation.

a. Low-temperature cirrus near the tropopause: 26 November 1995

Figure 3 shows the time–height variation of retrieved backscatter recorded by lidar for the period 1756–2200 local time (LT). Evidence from the observer's notes and from Japanese Geostationary Meteorological Satellite (GMS) imagery indicated that an anvil cloud had dissipated recently to reveal the observed layer. The time–height plot of cloud backscatter has a laminar appearance, although there is evidence of gravity waves throughout the layer. Around 1830 LT, the amplitude of such waves peaks at about 300 m. Figures 4a–h show the analyzed data in detail. Both the IR emittance in Fig. 4a and the integrated backscatter in Fig. 4c increase after 1800 LT but appear to peak at different times, indicating a change in ice-crystal characteristics with time. Figure 4d shows that much of the medium-term changes in radiance are caused by changes in the water vapor path, and the retrieved cloud radiance shown in Fig. 4e is about 5%–15% of the total measured radiance. The fundamental random noise in the IR radiometer detector signal and equivalent noise in water vapor path w translate into an rms noise value of ± 0.006 W m^{-2} sr^{-1}. This value represents the short-term minute-by-minute noise in Fig. 4e quite well. It is apparent that the analysis method will extract IR cloud radiances at a minimum level of less than 1% of the total radiance signal. As well as the random noise, systematic errors in the effective backscatter-to-extinction ratio $k/(2\overline{\eta})$ will result in errors in the retrieval of backscatter coefficient and infrared absorption coefficient. These and other errors are discussed in the appendix. The retrieved values of $2\alpha\overline{\eta}$ shown in Fig. 4f are discussed further in section 5c. The scatter in values of $\gamma'(\pi)$ when plotted against emittance is greater than estimated errors and indicates some change in ice-crystal characteristics, or of water vapor distribution, with time.

It is known that $k/(2\overline{\eta})$ might vary with temperature within a cloud. Single values of $k/(2\overline{\eta})$ for each lidar

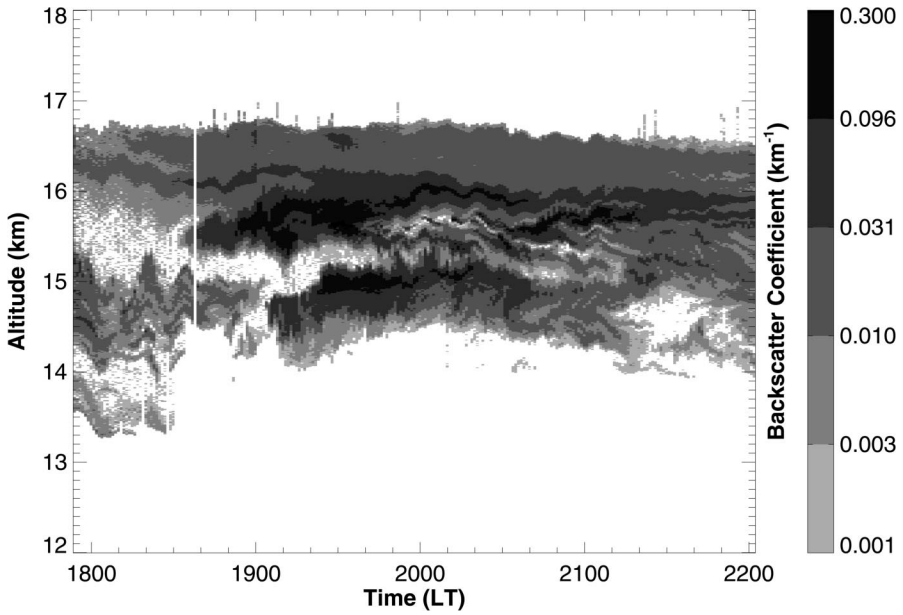

FIG. 3. Time–height image of lidar backscatter coefficient for a period on 26 Nov 1995.

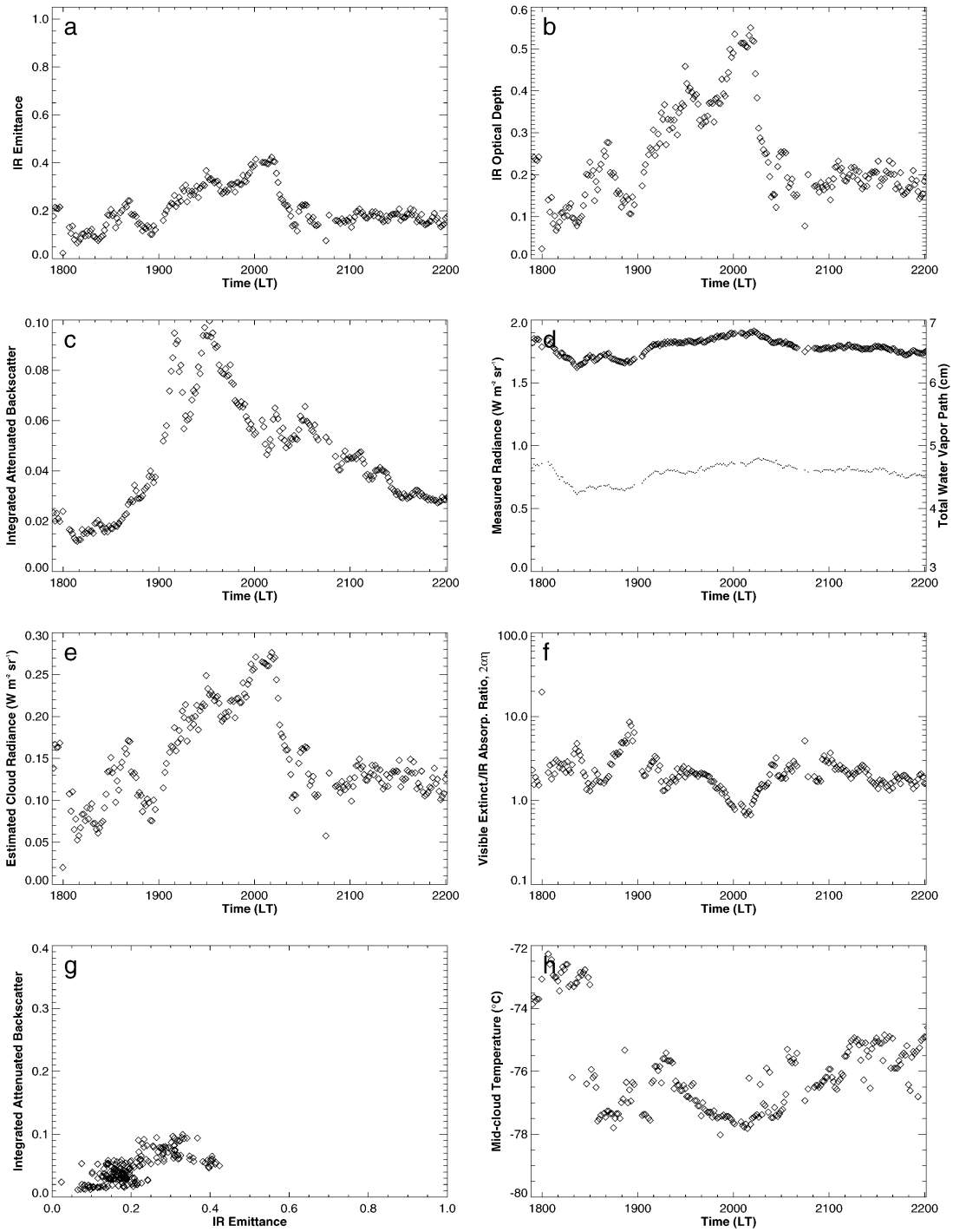

FIG. 4. Values of (a) IR absorption emittance ϵ_a, (b) IR absorption optical depth δ_a, (c) integrated attenuated backscatter $\gamma'(\pi)$, (d) measured IR radiance L_s (upper curve), and water vapor path w (lower curve), (e) retrieved cloud radiance L_c, (f) retrieved values of $2\alpha\overline{\eta}$, (g) $\gamma'(\pi)$ vs ϵ_a, and (h) midcloud temperature. The values are for the 26 Nov 1995 cloud in Fig. 3.

shot can be determined using the method of Sassen and Cho (1992) and Young (1995), by measuring the cloud transmittance as indicated by the deficit of molecular scattering above cloud top. However, for the high tropical clouds considered here, there was usually insufficient molecular backscatter above cloud top to make a sufficiently accurate measurement of transmittance.

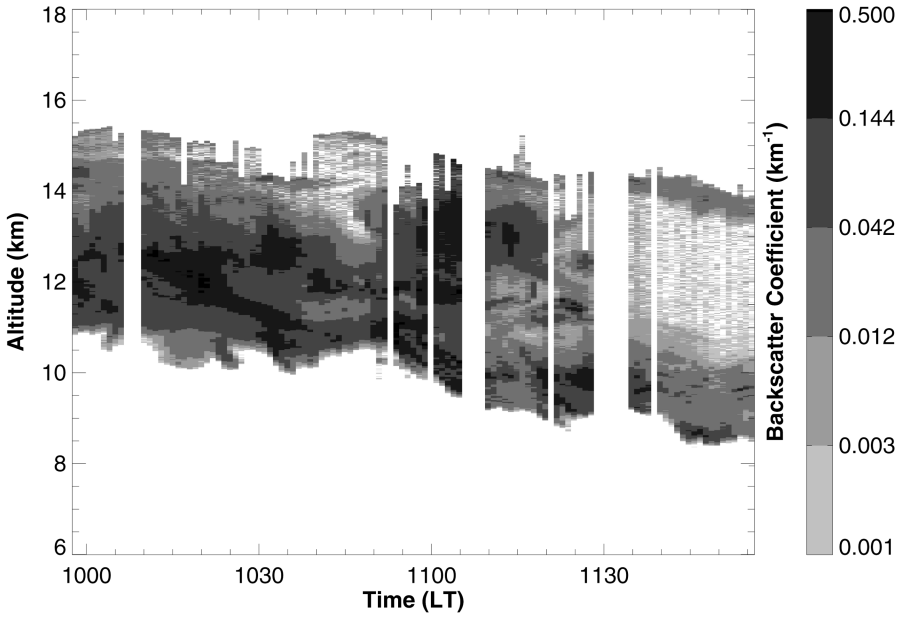

FIG. 5. Time–height image of lidar backscatter coefficient for a period on 5 Dec 1995.

b. Synoptic-type cirrus: 5 December 1995

Figures 5 and 6 illustrate data for 5 December 1995. The cloud was similar to those observed in midlatitudes, with the cloud base showing a slow descent from 11 to 8.5 km and the cloud depth varying between about 1.5 and 3 km. GMS imagery indicated that cirrus was fairly widespread at the time and may have been associated with a large convective disturbance about 300 km to the north. The IR absorption emittance ϵ_a varied from about 0.2 to 0.6, decreasing to less than 0.2 after 1100 LT. Values of $\gamma'(\pi)$ are better correlated with ϵ_a than in Fig. 4g. This is due partially to a lower uncertainty in ϵ_a but also reflects the presence of a more constant backscatter-to-extinction ratio $k/(2\overline{\eta})$ compared to Fig. 4g. It is also a result of a more constant water vapor path.

5. Dependence of cloud optical properties on temperature

A total of 34.4 h of data on emittance and other cloud properties of nonanvil cirrus, taken over 11 days, were sorted into cumulative midcloud temperature bins of 10°C width. Values measured in dissipating storm anvils were omitted and will be discussed in Part II. Exceptions were data from semitransparent parts of the storm anvils that were included in the higher temperature ranges, as described later.

a. Physical and infrared properties

Figure 7 shows statistics of cloud depth against temperature. In all cases, backscatter from the molecular atmosphere above cloud top could be discerned, so that no biases from fully attenuating clouds occurred. The bars indicate the standard deviation of sample values. The values agree quite well with the midlatitude values of Platt et al. (1987) and Sassen and Comstock (2001); however, the P98 values were much higher at the lower temperatures (~4 km at −80°C). Histograms of observed values of cloud absorption emittance ϵ_a and IR optical depth δ_a are shown in Figs. 8a and 8b. Compared to the PROBE values, there were fewer values with $\epsilon_a > 0.6$. Mean values of ϵ_a, $k/(2\overline{\eta})$, and σ_a as a function of temperature are shown in Fig. 9, along with similar mean values obtained previously on nonanvil cirrus in tropical and equatorial regions and cirrus in midlatitude regions. The MCTEX data exhibit much the same behavior as in previous experiments and extend the data to lower temperatures, where the optical quantities are seen to decrease further. The bars shown in Fig. 9a represent the standard deviation of the sample values in each bin. The random error in the means was much less. As an example, at −70°C and $\epsilon_a \approx 0.3$, the uncertainty in ϵ_a is about ±11%. This is much less than the standard deviation of measured emittance, as shown in Fig. 9a. Similar standard deviations in measured values were found in the PROBE data.

Some observations were also made on the integrated depolarization ratio Δ, and values are shown in Fig. 10. The values tend to decrease with temperature, as found in PROBE and in earlier studies. The values at −75°C to −80°C agree with those of P98 and Sassen and Benson (2001) for their results from the Facility for Atmospheric Remote Sensing (FARS), in Utah. However, they are slightly lower than the tropical cirrus values from Sassen and Benson (2001). An increase in Δ with height above cloud base, as found by Sassen et al. (2000), was also observed in the MCTEX data, although it is not illustrated here.

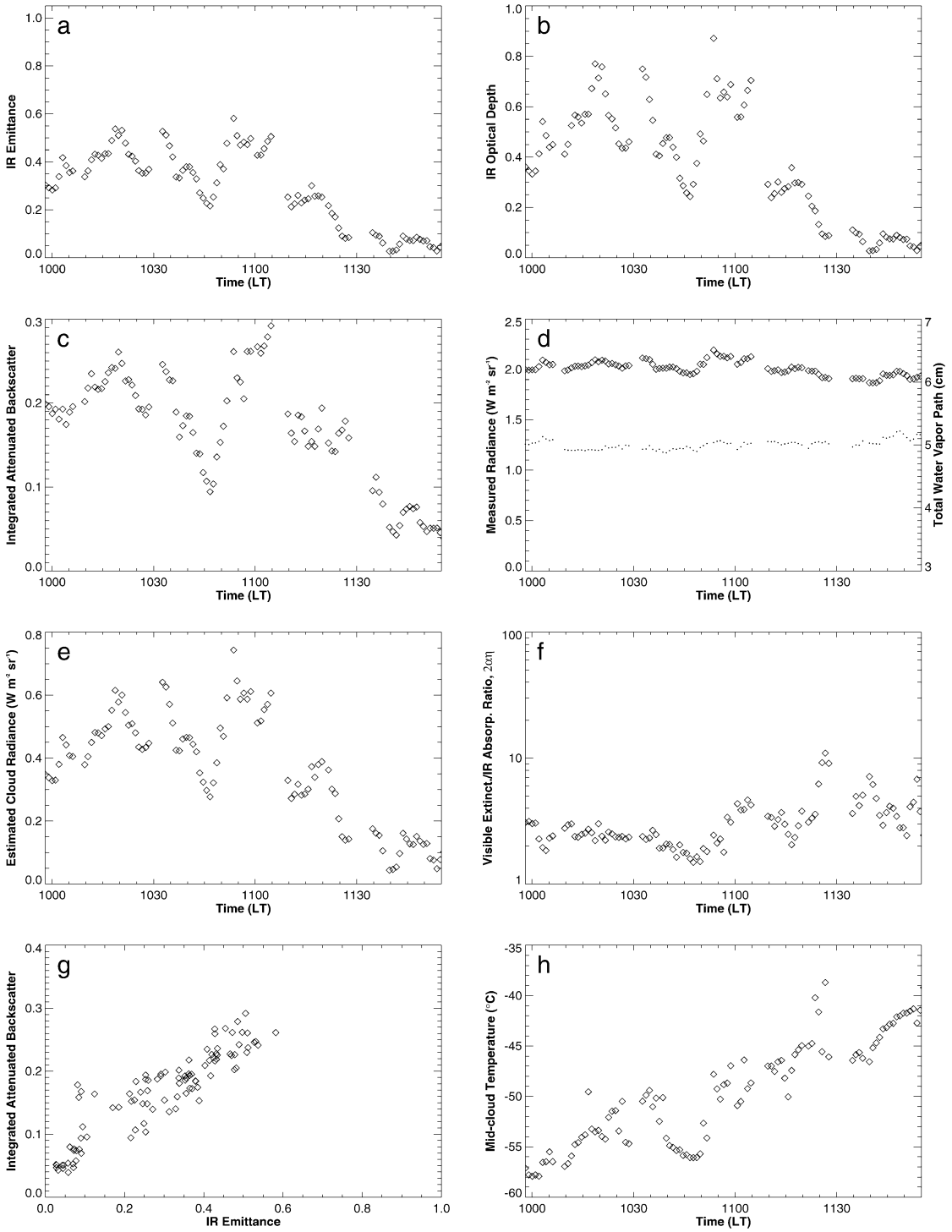

FIG. 6. As in Fig. 4, but for the 5 Dec 1995 cloud in Fig. 5.

Regressions were performed on the variations of ϵ_a and σ_a with temperature. Linear trends of the form

$$\epsilon_a = bT + \epsilon_o \tag{3}$$

(with T in degrees Celsius) were fitted to the midlatitude and Darwin synoptic data, the MCTEX and PROBE data, and the whole dataset, respectively. The constant ϵ_o gives the value of ϵ_a when $T = 0$°C. Values of b, ϵ_o, and regression coefficient R^2 are shown in Table 4. The correlation is seen to be good for midlatitude cirrus, but

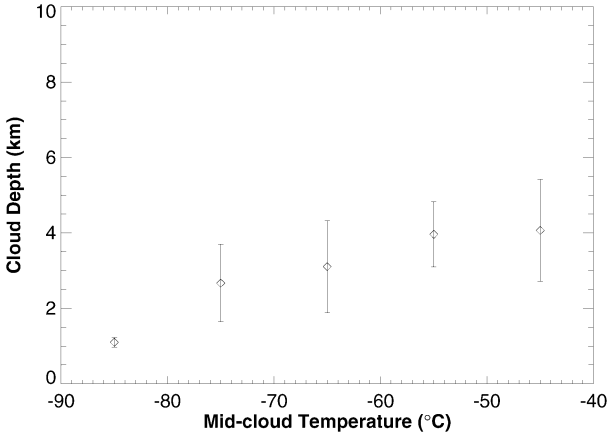

FIG. 7. Mean cloud depth vs temperature in 10°C intervals. Bars represent the std dev of individual samples.

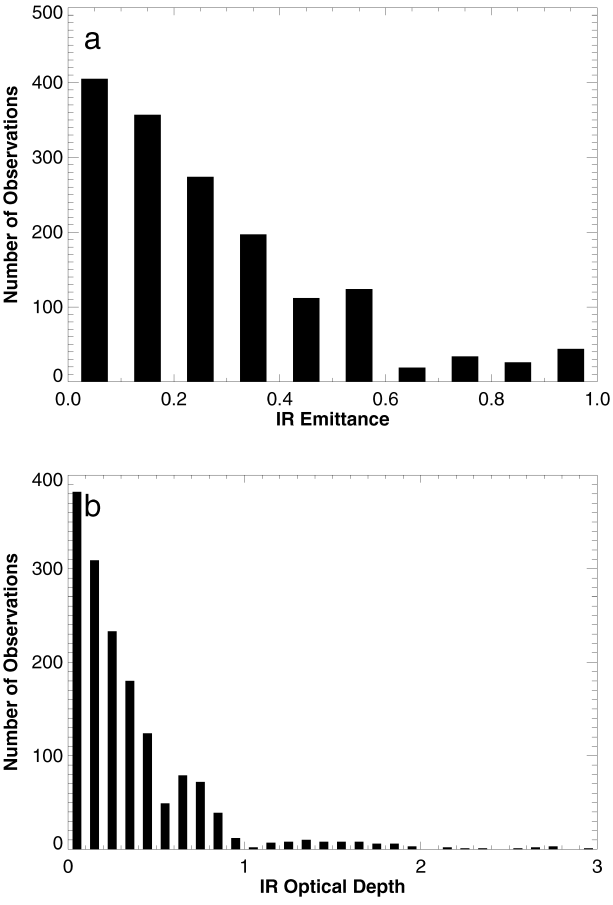

FIG. 8. Histograms of observed values of (a) emittance ϵ_a and (b) IR optical depth δ_a. Each observation represents a measurement at the time of each lidar profile as given in Table 2. Each profile was an average of up to 256 shots, at 10 Hz, and the IR measurement was taken at the center of the averaging period.

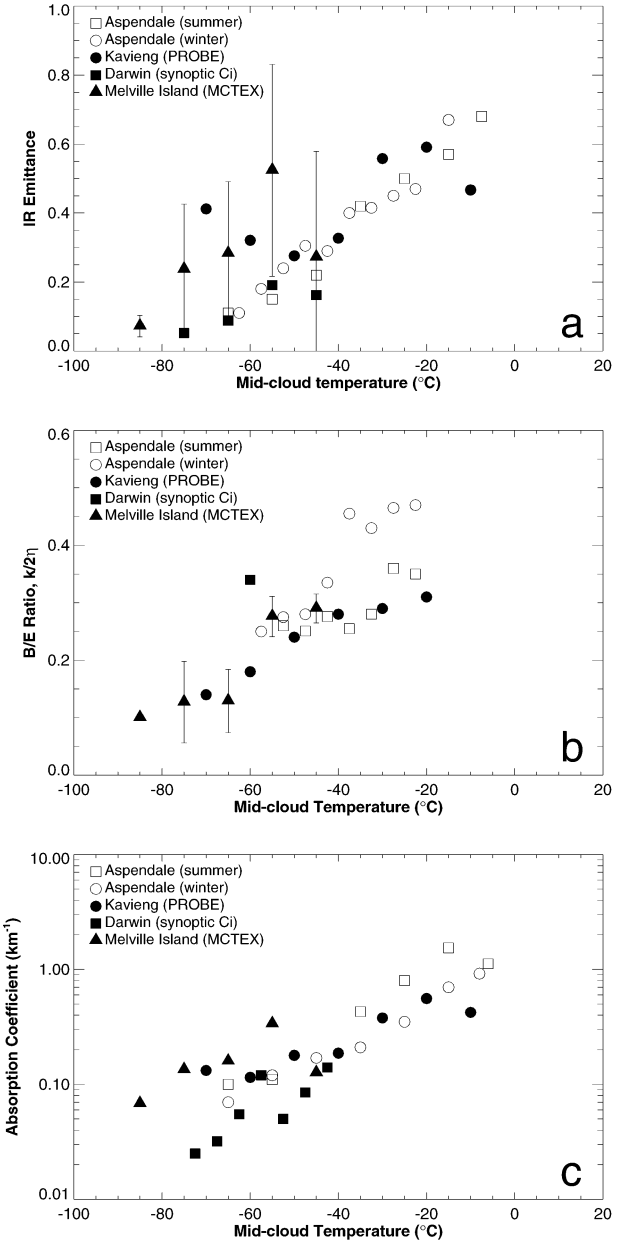

FIG. 9. Mean values of (a) ϵ_a, (b) $k/(2\overline{\eta})$, and (c) σ_a vs temperature in 10°C intervals. Aspendale summer and winter refer to Platt et al. (1987), Kavieng PROBE to Platt et al. (1998), and Darwin synoptic to Platt et al. (1984). Bars represent the std dev of samples in each interval.

the MCTEX and PROBE data are very scattered and also give much higher values of emittance at the lower temperatures (thus ϵ_o is similar but the slope is much less). The more fundamental value of absorption coefficient σ_a was also linearly correlated against temperature (Table 4). The correlation coefficient is higher than for the emittance, indicating that variability in cloud depth is contributing to the variability in ϵ_a. The absorption coefficient σ_a plotted against midcloud tem-

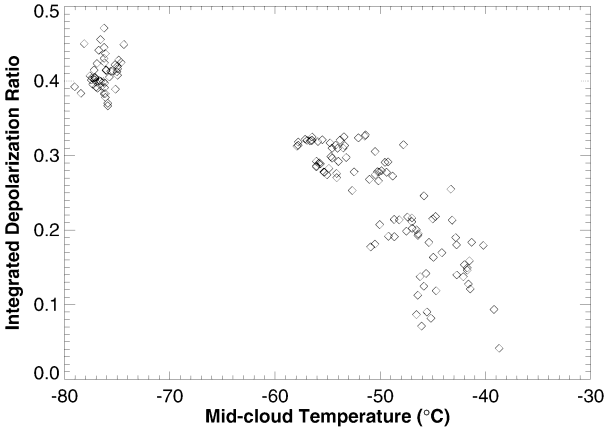

FIG. 10. Values of depolarization ratio vs midcloud temperature for some single profiles.

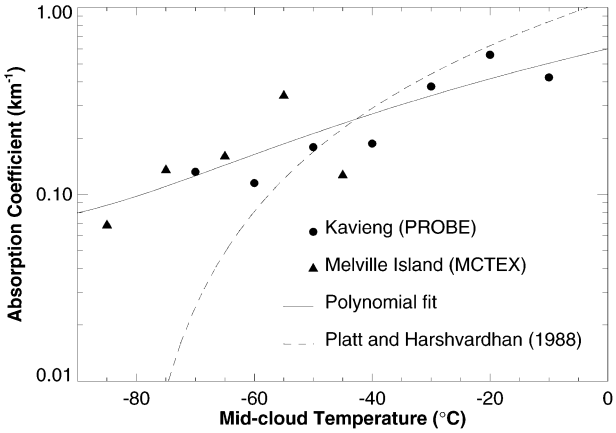

FIG. 11. Mean values of σ_a vs midcloud temperature for MCTEX and PROBE (Platt et al. 1998) data. The relation of Platt and Harshvardhan (1988) is also shown. The std dev of single samples is 0.07 at −70°C, 0.10 at −50°C, and 0.15 at −30°C.

perature is also shown in Fig. 11 for the MCTEX and PROBE values. A second-degree polynomial of the form

$$\sigma_a = AT^2 + BT + C \tag{4}$$

is shown fitted to the data. Values of A, B, C, and R^2 are shown in Table 4. The power-law curve fitted by Platt and Harshvardhan (1988) to the midlatitude and Darwin tropical synoptic cirrus data (Fig. 9c) is also shown.

Figure 9a shows that the emittance of tropical/equatorial clouds is systematically higher than that for midlatitude clouds, at least for temperatures below −50°C. From the regressions, there is a clear difference. At, say, −70°C, the tropical emittance is about 0.3 and midlatitude emittance about 0.1. The cloud depths appear to be somewhat greater in the tropical/equatorial cases, but the values of σ_a are also larger, as shown in Figs. 9c and 11. The reason for the larger values of σ_a at the lower temperatures lies in the likely greater ice contents at high altitudes in tropical clouds that are associated with convective storms. The higher ice content would be related to the ice particles and water vapor lifted to high altitudes by the intense convection found in both MCTEX and P98. As a contrast, the values of σ_a in tropical synoptic cirrus were more closely correlated to the values in midlatitude cirrus (Platt and Harshvardhan 1988). The recent values reported by Sassen and Comstock (2001) give σ_a equal to about 0.09 km^{-1} at both −70° and −60°C, and rising to 0.2 at −20°C. These are generally lower than the present work except at −70°C. Because these authors used the same LIRAD method, the differences might reflect different geographical locations.

The dataset is sufficient to give a guide for numerical models as to how ϵ_a and σ_a vary with temperature. The present dataset is presented as a limited, interim parameterization for tropical cirrus clouds before more comprehensive datasets are available. It should be pointed out, however, that tropical observations require extremely sensitive, low-noise, fast radiometers, together with a high-power lidar, such as were available in MCTEX.

A caveat that applies to all surface observations is that cirrus clouds are not detected by lidar and radiometry when lower clouds are present. As the low clouds can be diurnal in nature, some diurnal properties of cirrus will be missed.

b. Integrated attenuated backscatter and visible extinction to IR absorption ratio

Values of $\gamma'(\pi)$ plotted against ϵ_a are shown in Fig. 12 for two temperature intervals of −70° to −60°C and −30° to −20°C, respectively. Data for the latter temperature interval were taken from dissipating storm anvils to indicate behavior at the higher temperatures. Values of $k/(2\overline{\eta})$ and $\alpha\overline{\eta}$ retrieved from such curves for each temperature interval are shown in Table 5, with plus/minus uncertainties in the values shown in parentheses. Similarly, values in the −40° to −30°C range

TABLE 4. Coefficients in (3) and (4) determined for various regressions of ϵ_a and σ_a.

Data series	b	ϵ_0	R^2
ϵ_a (midlatitude and Darwin synoptic)	0.0099	0.737	0.943
ϵ_a (MCTEX and PROBE)	0.0048	0.606	0.518
ϵ_a (all data)	0.0072	0.657	0.671
σ_a (linear: MCTEX and PROBE)	0.0056	0.514	0.679
σ_a (polynomial: MCTEX and PROBE)	$A = 5 \times 10^{-5}$, $B = 0.0103$, $C = 0.6017$		0.707

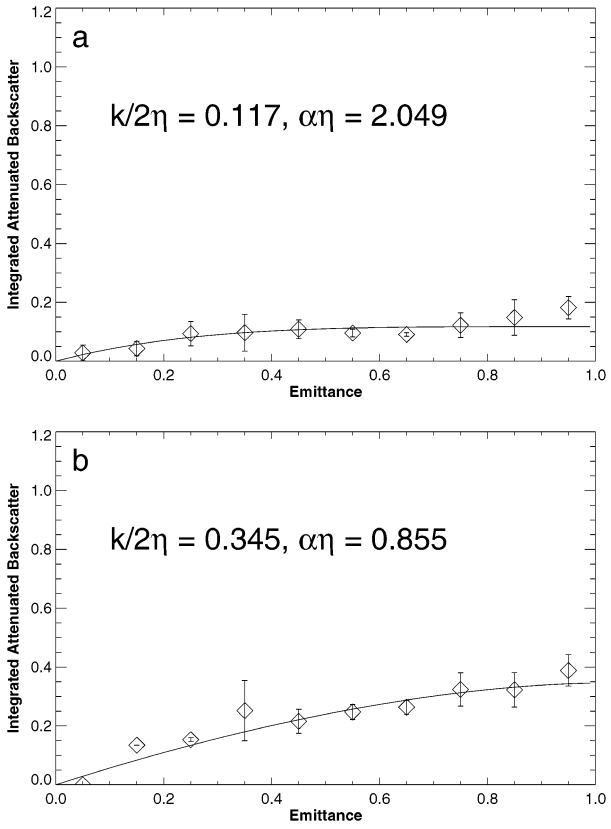

FIG. 12. Values of $\gamma'(\pi)$ vs ϵ_a for all nonanvil MCTEX retrievals in two temperature intervals: (a) $-70°$ to $-60°$C and (b) $-30°$ to $-20°$C.

included data from dissipating storm anvil clouds, mainly to illustrate how α and $\overline{\eta}$ behaved at the higher temperature range. Values of $k/(2\overline{\eta})$ are also shown in Fig. 9b.

Values of k and α were then calculated using values of $\overline{\eta}$ discussed in section 3d, and results are shown again in Table 5. Values of k are seen to increase with temperature; however, because of the higher values of $\overline{\eta}$ now used, the values of k are now higher than those shown in P98 for PROBE. Values of α are discussed in the next section.

c. Retrieval of effective diameter D_e

Values of D_e were retrieved from the curve of α versus D_e shown in Fig. 2 using the values of α shown in Table 5. The values of $\overline{\eta}$ chosen, as shown in Table 5, reflect the uncertainty in our present state of knowledge. We use values equal to 0.6 ± 0.1 for the lower temperature ranges and 0.41 ± 0.02 for the two higher ranges. A consideration in choosing these values was that $\overline{\eta}$ must also be consistent with the retrieved values of D_e. For example, the value of α calculated for the $-40°$ to $-30°$C range is quite accurate (for large particles found in dissipating anvils) if the value of $\overline{\eta}$ is equal to 0.41, but will be quite unrealistic if a value of 0.6 is used. Similarly, the value of $\overline{\eta}$ used in the $-80°$ to $-70°$C range gives a value of D_e that is consistent with the phase function used, but would be too small if a value of $\overline{\eta}$ equal to 0.41 was used. For intermediate temperature ranges, values of $\overline{\eta}$ used are approximately consistent with particle size. The value of α in the $-50°$ to $-40°$C range is probably too high due to large error, and the value of D_e should lie somewhere between the values of the adjacent ranges. Thus, the values of $\overline{\eta}$ given by Platt (1981) for the large-particle cirrus model give consistent values of α at the higher temperatures, whereas the values of α, and thus of D_e, at the lower temperatures are more consistent with the values of $\overline{\eta}$ that are obtained at those temperatures. In reality, $\overline{\eta}$ will change with temperature more monotonically between the large- and small-particle values. However, because the particle size is being retrieved, rather than provided, such information is not available at present. A more comprehensive and detailed study of particle size and multiple scattering factors is planned.

Finally, values of α calculated by Mitchell et al. (1999) for a range of temperatures are shown in the final column of Table 5. These values are based on various experimental data, as described in their paper. Values of α and k recalculated from the PROBE data are shown in Table 6. The PROBE (P98) values of α are now lower, and the values of D_e are consequently higher, and comparable with the values in Table 5. The examples above indicate that with better and more representative values of $\overline{\eta}$ for a range of values of α, quite accurate values of D_e should be possible. Recent values of α reported by Sassen and Comstock (2001) vary between about 2.2 at $-30°$C and 2.8 at $-60°$C, in approximate agreement with the present results.

It should be noted that because of the actual variation of $\eta(z)$ at the lower cloud optical and geometrical depths, the relation between $\gamma'(\pi)$ and ϵ_a will give a

TABLE 5. Values of $k/(2\overline{\eta})$, $2\alpha\overline{\eta}$, and $\overline{\eta}$, and calculated values of k, α, and D_e in MCTEX. T_{mc} is the midcloud temperature.

T_{mc} (°C)	$k/2\overline{\eta}$	$\overline{\eta}$	k	$2\alpha\overline{\eta}$	α	D_e^* (μm)	α^{**}
−75	0.10 ± 0.02	0.6 ± 0.1	0.12 ± 0.02	4.31 ± 0.05	3.6 ± 1.3	(5.3–30)	3.96
−65	0.12 ± 0.02	0.6 ± 0.1	0.14 ± 0.03	4.10 ± 0.05	3.4 ± 1.1	8.7 (5.4–18)	3.05
−55	0.22 ± 0.02	0.6 ± 0.1	0.27 ± 0.05	4.00 ± 0.05	3.3 ± 0.9	9.3 (6.8–20)	2.54
−45	0.22 ± 0.03	0.60 ± 0.15	0.26 ± 0.08	6.00 ± 0.05	4.4 ± 1.5	8 (4–11)	2.27
−35	0.38 ± 0.03	0.41 ± 0.02	0.32 ± 0.08	1.6 ± 0.2	2.0 ± 0.5	(~80–100)	2.1

* Values in parentheses show range of effective diameters for the given uncertainties.
** Values from aircraft observations (see text).

TABLE 6. As in Table 5, with modified PROBE values of $\overline{\eta}$ (see text).

T_{mc} (°C)	$k/2\overline{\eta}$	$\overline{\eta}$	k	$2\alpha\overline{\eta}$	α	D_e (μm)
−70	0.14 ± 0.02	0.6 ± 0.1	0.17 ± 0.03	2.90 ± 0.05	2.4 ± 0.8	17 (8–100)
−60	0.18 ± 0.02	0.6 ± 0.1	0.22 ± 0.04	3.40 ± 0.05	2.8 ± 0.9	11 (7–100)
−50	0.22 ± 0.03	0.6 ± 0.1	0.26 ± 0.04	3.60 ± 0.05	3.0 ± 0.9	10.5 (7–80)
−40	0.29 ± 0.03	0.41	0.35 ± 0.06	1.7 ± 0.2	2.1 ± 0.7	>100

slightly different curve than when $\eta(z)$ is constant ($=\overline{\eta}$). An investigation of this effect, following Platt et al. (1987), indicated that retrieved values of α, assuming a *constant* effective $\overline{\eta}$, would be about 10% lower. Equivalent corrections were made to the values of α.

d. Visible optical depth, 532 nm

The high values of α in the colder clouds, as evident from Table 6, imply that the visible extinction optical depth δ_c could be 2.5–4 times the IR optical depth δ_a. This arises physically because the IR absorption efficiency decreases for particle sizes less than about 20 μm. In daytime conditions, the solar albedo should then be enhanced significantly over the IR absorption compared to warmer cirrus clouds, thus pushing the radiation balance of the clouds toward a cooling at the surface (e.g., Platt 1981; Stephens et al. 1990). It also implies that, because the value of δ_a is often significant, the number density of particles in the cloud must be high. Results in Fig. 8b indicate values of δ_a up to unity or greater, although they are frequently less than 0.5. A histogram of values of δ_c, similar to that for δ_a in Fig. 8b, is shown in Fig. 13, where the number of occurrences is plotted against the interval in visible optical depth. The number of cases where δ_c is greater than unity is about 27% of the total. The histogram bears considerable resemblance to the PROBE case in P98. Measurements of optical depths up to 4 are realistic because the multiple scattering factor $\overline{\eta}$ is approximately 0.5. The corresponding two-way cloud transmittance for an optical depth of 4 is 0.02, which can still be measured by the lidar.

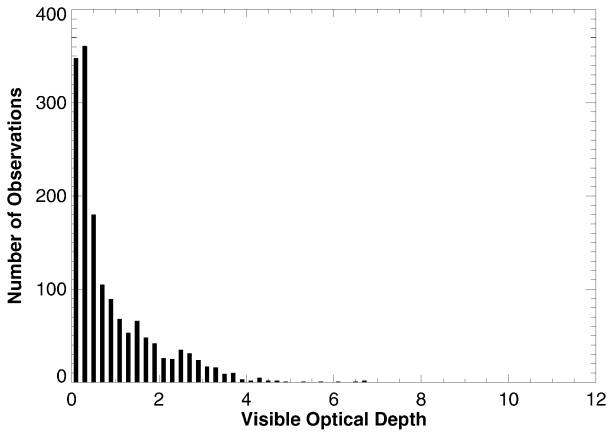

FIG. 13. Histogram of cirrus visible optical depth δ_c for nonanvil MCTEX cases.

6. Discussion and conclusions

This is the first paper to examine a number of high, cold tropical cirrus layers with the LIRAD method. These are also the first observations at a site where ''island thunderstorms'' occur. Such thunderstorms make up a large percentage of convection in the large island areas north and east of Australia. Many of the results are similar to those in PROBE (P98) at a site much closer to the equator. The measured cloud depths of about 3–4 km are similar to those observed in P98 except at the lowest temperatures, where the P98 values were greater. The depths tend to be greater than for midlatitude clouds (e.g., Platt et al. 1987). The histograms of ϵ_a and σ_a, in terms of numbers of observations, indicate the preponderance of emittances below 0.6 and IR optical depths below 1. In fact, the cutoff in optical depths above a value of 1 is quite striking. The clouds in P98 gave a greater frequency of both higher emittances and IR optical depths, with a second peak at about 1.4. The values of σ_a in MCTEX and P98 are much higher at the lower temperatures (below −40°C, for P98) compared to midlatitude clouds. As stated earlier, this must reflect greater relative humidity, due to the intense convection in the Tropics, with similarly greater variations in the tropical upper troposphere compared to midlatitudes.

Values of $k/(2\overline{\eta})$ tend to be similar to those found in P98, particularly at the lowest temperatures. In fact, the present data lend credence to the low values of $k/(2\overline{\eta})$ in the −80° to −60°C temperature range that were found in P98 (this is still true after recalculation of the values of k). The values of k shown in Table 5 demonstrate the typical change in this quantity with temperature, providing useful information in terms of temperature for some purposes. The values agree quite well with those of Sassen and Comstock (2001), for midlatitude cirrus in the United States, who also find a dependence on temperature. The values can be compared with values obtained theoretically for various ice-crystal habits shown in Table 7, as was also done in Platt et al. (1998). Some theoretical values appear to be too high, as found in P98. Recent models have demonstrated the effects of placing artificial imperfections in a hexagonal crystal structure. Macke and Mischenko (1996) found that a 5%–15% distortion in regular hexagonal crystals re-

TABLE 7. Theoretical values of k for variously distorted crystals.

(a) Macke and Mischenko (1996): Distorted hexagonal column

T (distortion factor)	k aspect ratio 5	k aspect ratio 0.2
5%	0.35	0.3
10%	0.10	0.07
15%	0.08	0.07

(b) Hess et al. (1998): Distorted hexagonal column

θ (change in tilt of one surface)	k	Δ
0°	0.3	0.67
10°	0.2	0.33
30°	0.15	0.48
90°	0.12	0.33

(c) Macke et al. (1996): Distorted polycrystal

Distortion	k
2%	0.8
6%	0.3
14%	0.14
18%	0.07

duced k from 0.35 to 0.08. Hess et al. (1998) found that equivalent distortions in the tilted plane of reflection for 10°–30° tilt planes reduced k from 0.2 to 0.12. Similarly, Takano and Liou (1995) determine a large decrease (0.9–0.09) when a hollow column replaces a solid hexagonal column. Macke et al. (1996) also obtain a decrease in k when a second-generation Koch fractal is distorted. Recently, Yang and Liou (1996), using an advanced technique, found that reducing the size of the hexagonal crystals also reduced the value of k considerably. In fact, the solid column with length 11 μm has a value of k of 0.035, which is generally lower than the MCTEX values. There is a paucity of theoretical data for the depolarization ratio Δ for comparison with observation. Hess et al. (1998) provided scattering matrix elements from which values of Δ could be computed. These are also shown in Table 7. They compare approximately with experimental values. However, although values of k vary strongly with temperature, Hess et al. (1998) show no correlation between k and corresponding values of Δ.

It is apparent that there is still a good deal of ambiguity in the k and Δ values for different crystal types and distortions. Distorted hexagonal crystals, hollow columns, bullet rosettes, and distorted fractals can all be made to agree with observed values with the right amounts of distortion. Values associated with these distorted habits are certainly more realistic than the higher values in the region of 0.9–1.0 obtained theoretically for larger solid hexagonal columns. Because of the above ambiguity, several independently measured parameters will be required to determine the most realistic model. The depolarization ratio is a quantity that should be calcualted along with the cloud particle scattering phase functions. Another parameter that can be tested is the asymmetry parameter. There are instruments that can obtain this quantity from cloud in situ measurements. Similarly, the measured angular distribution of scattered solar radiance can provide some discrimination (e.g., Francis et al. 1999).

The relations reported here for ϵ_a and σ_a in terms of temperature provide up-to-date quantities for validation of cloud relationships in climate models or cloud-resolving models. A caveat here is that tropical cirrus observations were biased toward nighttime periods and also morning periods before the buildup of cumulus clouds. Thus, some diurnal effects might possibly have been missed.

An examination of α, the ratio of visible extinction coefficient to IR absorption coefficient, indicates a systematic increase, within the ranges of uncertainty, as the cloud temperature decreases. Using recent theoretical calculations on various ice-crystal habits, it is found that the increase in α can be explained by a decrease in the effective diameter of the ice-crystal size distribution. The variation in α is found to agree quite well with past observations. These large values indicate small ice crystals, of the order of 10-μm effective diameter, or less. There are valid reasons for a considerable decrease in crystal size at temperatures near the tropical tropopause. The theory of the evolution and origin of such layers has been discussed by Jensen et al. (1996); their theory indicates that cirrus layers that can be long-lasting are composed of ice crystals less than 10 μm in size. Jensen et al. (1996) consider two possible sources for such layers. The first is advection of a layer from a tropical storm anvil just below the tropopause. The larger particles fall out rapidly leaving a cloud layer of small crystals that remains at about the same altitude and thickness for many hours. The MCTEX thunderstorms (Keenan et al. 2000) took from 4 to 7 h to dissipate sufficiently before LIRAD studies could be made (Part II). Preliminary results shown in Keenan et al. (2000) indicated that particles up to 0.8 mm in size were lifted to a 17-km altitude. Using expressions for fall velocity from Heymsfield (1975), we calculated ice-crystal sizes (e.g., bullets) remaining in a cloud 1 km deep after certain time periods from maximum convection. The largest sizes remaining in such a cloud are 160, 100, 80, and 66 μm after 2, 4, 6, and 8 h, respectively. For a typical bimodal size distribution as discussed by Mitchell and Platt (1999), this implies that after about 6 h only the smaller mode, with mean diameter of 10 μm, remains. Thus, it is possible that the clouds observed were remnants of thunderstorms, as postulated by Jensen et al. (1996). These layers can even possess high optical depths if sufficient nuclei are available.

The second source model considered by Jensen et al. (1996) allows cloud nucleation and formation through some sort of lifting mechanism, such as gravity waves or infrared warming. Such layers would assume optical depths of no more than about 0.05 because of the restricted vertical extent and slow uplift.

The infrared extinction values obtained by Rinsland

et al. (1998) at different IR wavelengths through occultation spectra also indicated cloud particles of about 12-μm diameter in clouds in the tropical atmosphere from 13- to 16-km altitude.

The cloud layers observed in MCTEX had quite high visible optical depths at times, and the convective anvil origin would appear to fit the observations better. This is particularly true because the observed cloud layers could be quite deep and the generation of storm anvils over the Tiwi Islands occurred on most days.

The high optical depths and small particle sizes typical of the MCTEX clouds leads to relatively high number densities in the clouds. We can estimate these by taking typical values of σ_a (0.1–0.2 km^{-1}) and α (3–3.6) to give extinction coefficients approximately in the range of 0.4–0.6 km^{-1}. Equivalent number densities are then 5–9 cm^{-3} for 10-μm-size particles. As a comparison, Knollenberg et al. (1993) measured number densities of the order of 100 cm^{-3} in the particle size range from 1 to 10 μm, so that the MCTEX numbers do not appear to be excessive.

Acknowledgments. The authors wish to acknowledge the following: The Tiwi Islands Land Council for permission to make observations on Melville Island; our colleagues at Aspendale for assistance, particularly in the Engineering and Electronics Workshops; and the Bureau of Meteorology for organizing the overall MCTEX campaign. Stephen Marsden made a preliminary analysis of the data. The field observations and part of the salaries were funded by U.S. Department of Energy, Office of Health and Environmental Research, Grants DE-FG02-92ER61373 and DE-FG03-94ER61748. The authors are also grateful to two anonymous reviewers whose comments and criticisms have led to some important changes and additions that have improved the paper considerably.

APPENDIX

Uncertainties in ϵ_a and σ_a

A detailed discussion of calibration procedures and experimental uncertainties was given in P98. This section gives additional information pertinent to the MCTEX data and for the new CSIRO/ARM radiometer and calibration procedure employed.

a. Calibration

As stated previously, radiometer calibration was accomplished with two blackbody sources at different temperatures. This two-point calibration eliminated effects due to drift in the reference blackbody temperature and to residual emission from the scanning mirror. Remaining systematic errors arose from errors in the measured temperatures of the two blackbodies. The liquid nitrogen (LN_2) source was treated as a ''zero-radiance'' (77 K) blackbody. Because any mist of condensed ice crystals above the liquid surface was found to cause the brightness temperature to increase by about 1°C maximum, great care was taken to ensure that the liquid looked perfectly clear at the time of calibration. Corrections were made for the measured nonblackness of the submerged blackened cone (the LN_2 was found experimentally to have an emittance of about 0.9, but this improved to better than 0.99 with the cone). The residual uncertainty was considered to be about 0.1°C. In the ice–water mixture, the temperature of the water was found to be typically about 0.2°–0.3°C above freezing. This temperature was measured at each calibration. The residual uncertainty was again considered to be about 0.1°C.

TABLE A1. Uncertainties in ϵ_a and δ_a.

		$\Delta\delta_a/\delta_a = \Delta\epsilon_a/\epsilon_a$ random error			
δ_a	ϵ_a	−80°C	−70°C	−60°C	−50°C
0.2	0.18	0.21	0.152	0.11	0.085
0.4	0.33	0.13	0.093	0.067	0.052
0.6	0.45	0.11	0.076	0.055	0.042
0.8	0.55	0.097	0.069	0.05	0.039
1.0	0.63	0.094	0.068	0.049	0.038

b. Random errors in measured radiance and water vapor path

The Noise Equivalent Power of the CSIRO/ARM radiometer was reduced by a factor of about 30 from that of the CSIRO Mark II radiometer used in P98. Thus, random noise from the radiometer was no longer a dominant source. Random fluctuations in water path were obtained from J. Liljegren (1999, personal communication). The rms values were again changed to the averaging times considered and then multiplied by the current normalization ratio, L_{sky}/w.

Errors can also occur through incorrect values of the radiance L_{sky} and transmittance τ in the retrieval of L_c. These quantities are calculated with a radiative transfer equation at the time of each radiosonde. Where possible, they are normalized to an experimental value of L_{sky}, if there is a cloudless patch of sky, by varying the value of the continuum absorption coefficient. Otherwise, L_{sky} is varied by plotting $\gamma'(\pi)$ versus L_c as discussed in section 3b. A related uncertainty can occur through any change in distribution of water vapor with height between radiosonde observations. Calculation of L_{sky} and τ from all radiosonde cases gives a fairly tight relationship, as given in (1). Nevertheless, the above-mentioned uncertainties could be quite appreciable and are included in Table A1.

c. Systematic errors in the calculation of cloud emittance

Any error in $k/(2\overline{\eta})$ will cause a distortion in the cloud backscatter profile and a change in the calculated emit-

tance. Simulations of this effect were made originally by Platt (1979) and were shown to be significant, particularly at higher values of emittance. Further simulations were made using the MCTEX data, obtaining the sensitivity of the calculated value of ϵ_a to varying $k/(2\overline{\eta})$.

d. Total estimated uncertainties

The total estimated errors in cloud emittance and optical depth varied from about 0.22 for a temperature of -80°C and $\epsilon_a \approx 0.2$ to about 0.11 for a temperature of -50°C and $\epsilon_a \approx 0.8$. The random noise level is independent of signal strength, so that the random component becomes a smaller percentage of the total as the emittance and/or temperature increases. The systematic component increases with δ_a or ϵ_a because the retrieval error increases nonlinearly with optical depth. At higher temperatures, the systematic component dominates, and the dependence of the fractional error on the optical depth becomes weak.

e. Errors in the calculation of α

The quantity $\alpha\overline{\eta}$ was retrieved in a similar manner to that of P98. The points in a plot of $\gamma'(\pi)$ versus ϵ_a, as shown in Fig. 12, were fitted by a curve given by (7) in P98. This is the standard equation used in the LIRAD method. This method has the advantage of utilizing the average values of $\gamma'(\pi)$ and ϵ_a, thus reducing the uncertainties from random noise and systematic uncertainties in individual values. It also has the advantage of avoiding a retrieval of α from individual IR and visible optical depth values, the latter of which are prone to large errors (Platt 1979). An estimation of residual uncertainty in the values of $\alpha\overline{\eta}$ is given by the values in parentheses in Table 5. The figures represent the sum of uncertainties due to error in the values of $\overline{\eta}$, and uncertainties in the retrieval of $\alpha\overline{\eta}$ from the $\gamma'(\pi) - \epsilon_a$ curve that includes errors in both the measurement of $\gamma'(\pi)$ and the calculation of ϵ_a. These uncertainties were estimated by detailed simulation. The errors in $\gamma'(\pi)$ and ϵ_a were estimated as in P98 and earlier in sections Ab–Ad. The uncertainties in α shown in Table 5 lead to the range of values of effective diameter D_e, which is also shown in Table 5.

A similar treatment was given to the previous values from P98 (Table 6).

REFERENCES

Baran, A. J., P. N. Francis, L.-C. Labonnote, and M. Doutriaux-Boucher, 2001: A scattering phase function for ice cloud: Tests of applicability using aircraft and satellite multi-wavelength radiance measurements of cirrus. *Quart. J. Roy. Meteor. Soc.*, **127,** 2395–2416.

Bissonette, L. R., and Coauthors, 1995: LIDAR multiple scattering from clouds. *Appl. Phys.*, **60B,** 355–362.

Clough, S. A., F. X. Kneizys, and R. W. Davies, 1989: Line shape and the water vapour continuum. *Atmos. Res.*, **23,** 229–241.

Francis, P. N., J. S. Foot, and A. J. Baran, 1999: Aircraft measurements of the solar and infrared properties of cirrus and their dependence on ice crystal shape. *J. Geophys. Res.*, **104,** 809–848.

Gates, W. L., and Coauthors, 1999: An overview of the results of the Atmospheric Model Intercomparison Project (AMIP I). *Bull. Amer. Meteor. Soc.*, **80,** 29–56.

Hess, M., R. B. A. Koelemeijer, and P. Stamnes, 1998: Scattering matrices of imperfect hexagonal crystals. *J. Quant. Spectrosc. Radiat. Transfer*, **60,** 301–308.

Heymsfield, A. J., 1975: Cirrus uncinus generating cells and the evolution of cirriform clouds. Part I: Aircraft observations of the growth of the ice phase. *J. Atmos. Sci.*, **32,** 799–808.

Jensen, E. J., O. B. Toon, H. B. Selkirk, J. D. Spinhirne, and M. R. Schoeberl, 1996: On the formation and persistence of subvisible cirrus clouds near the tropical tropopause. *J. Geophys. Res.*, **101,** 21 361–21 375.

Keenan, T., and Coauthors, 1994: Science plan for the Maritime Continent Thunderstorm Experiment (MCTEX). BMRC Research Rep. 44, Melbourne, Victoria. Australia, 61 pp. [Available from Bureau of Meteorology, BMRC, P. O. Box 1289k, Melbourne, Victoria 3001, Australia.]

——, and Coauthors, 2000: The Maritime Continent Thunderstorm Experiment (MCTEX): Overview and some results. *Bull. Amer. Meteor. Soc.*, **81,** 2433–2455.

Knollenberg, R. G., K. Kelly, and J. C. Wilson, 1993: Measurements of high number densities of ice crystals in the tops of tropical cumulonimbus. *J. Geophys. Res.*, **98,** 8639–8664.

Lee, A. C. L., 1973: A study of the continuum absorption within the 8–13 μm window. *Quart. J. Roy. Meteor. Soc.*, **99,** 490–505.

Liljegren, J. C., 1994: Two-channel microwave radiometer for observations of total column precipitable water vapor and cloud liquid water path. Preprints, *Fifth Symp. on Global Change Studies*, Nashville, TN, Amer. Meteor. Soc., 262–269.

Macke, A., and M. I. Mischenko, 1996: Applicability of regular particle shapes in light scattering calculations for atmospheric ice particles. *Appl. Opt.*, **33,** 4291–4296.

——, J. Mueller, and E. Raschke, 1996: Single scattering properties of atmospheric ice crystals. *J. Atmos. Sci.*, **53,** 2813–2825.

Mitchell, D. L., 2000: Parameterization of the Mie extinction and absorption coefficients for water clouds. *J. Atmos. Sci.*, **57,** 1311–1326.

——, and C. M. R. Platt, 1999: Microphysical interpretation of LIRAD extinction/absorption ratios using a microphysics-radiation scheme. *Proc. Eighth ARM Science Team Meeting*, Tucson, AZ, U.S. Department of Energy, 495–498.

——, S. Chai, Y. Liu, A. J. Heymsfield, and Y. Y. Dong, 1996: Modeling cirrus clouds. Part I: Treatment of bimodal size spectra and case study analysis. *J. Atmos. Sci.*, **53,** 2952–2966.

——, D. Ivanova, J. M. Edwards, and G. M. McFarquhar, 1999: A GCM parameterization of bimodal size spectra for ice clouds. *Proc. Ninth ARM Science Team Meeting*, San Antonio, TX, U.S. Department of Energy. [Available online at http://www.arm.gov/docs/documents/technical/conf_9903/mitchell(2)-99.pdf.]

Platt, C. M. R., 1979: Remote sounding of high clouds. I: Calculation of visible and infrared optical properties from lidar and radiometer measurements. *J. Appl. Meteor.*, **18,** 1130–1143.

——, 1981: Remote sounding of high clouds. Part III: Monte Carlo calculations of multiple scattered lidar returns. *J. Atmos. Sci.*, **38,** 156–167.

——, 1997: A parameterization of the visible extinction of ice clouds in terms of the ice/water content. *J. Atmos. Sci.*, **54,** 2083–2098.

——, and G. L. Stephens, 1980: The interpretation of remotely sensed high cloud emittances. *J. Atmos. Sci.*, **37,** 2314–2322.

——, and Harshvardhan, 1988: Temperature dependence of cirrus extinction: Implications for climate feedback. *J. Geophys. Res.*, **93,** 11 051–11 058.

——, A. C. Dilley, J. C. Scott, I. J. Barton, and G. L. Stephens, 1984: Remote sounding of high clouds. V: Infrared properties and

structure of tropical thunderstorm anvils. *J. Climate Appl. Meteor.,* **23,** 1296–1308.

——, J. C. Scott, and A. C. Dilley, 1987: Remote sounding of high clouds. VI: Optical properties of midlatitude and tropical cirrus. *J. Atmos. Sci.,* **44,** 729–747.

——, J. W. Bennett, S. A. Young, M. D. Fenwick, P. J. Manson, G. R. Patterson, and B. Petraitis, 1993: Narrow-beam fast filter radiometry and the use of the Lidar/Radiometer method in the Atmospheric Radiation Measurement Program. *Proc. Third ARM Program Science Team Meeting,* Norman. OK, U.S. Department of Energy, Office of Energy Research, Office of Health and Environmental Research, Environmental Sciences Division, 293–297.

——, S. A. Young, P. J. Manson, G. R. Patterson, S. C. Marsden, R. T. Austin, and J. Churnside, 1998: The optical properties of equatorial cirrus from observations in the ARM Pilot Radiation Observation Experiment. *J. Atmos. Sci.,* **55,** 1977–1996.

——, R. T. Austin, S. A. Young, and A. J. Heymsfield, 2002: LIRAD observations of tropical cirrus clouds in MCTEX. Part II: Optical properties and base cooling in dissipating storm anvil clouds. *J. Atmos. Sci.,* **59,** 3163–3177.

Rinsland, C. P., and Coauthors, 1998: ATMOS/ATLAS3 infrared profile measurements of clouds in the tropical and subtropical atmosphere. *J. Quat. Spectrosc. Radiat. Transfer,* **60,** 903–919.

Sassen, K., and B. S. Cho, 1992: Subvisual-thin cirrus lidar dataset for satellite verification and climatological research. *J. Appl. Meteor.,* **31,** 1275–1286.

——, and S. Benson, 2001: A midlatitude cirrus cloud climatology from the Facility for Atmospheric Remote Sensing. Part II: Microphysical properties derived from lidar depolarization. *J. Atmos. Sci.,* **58,** 2103–2112.

——, and J. M. Comstock, 2001: A midlatitude cirrus cloud climatology from the Facility for Atmospheric Remote Sensing. Part III: Radiative properties. *J. Atmos. Sci.,* **58,** 2113–2127.

——, R. P. Benson, and J. D. Spinhirne, 2000: Tropical cirrus cloud properties from TOGA/COARE airborne polarization lidar. *Geophys. Res. Lett.,* **27,** 673–676.

Schmitt, C. G., R. P. Lawson, and B. A. Baker, 2000: In situ measurements of mid-latitude and tropical cirrus clouds. *Proc. of the 13th Int. Conf. on Clouds and Precipitation,* Reno, NV, Int. Commission on Clouds and Precipitation of the Int. Association of Meteorology and Atmospheric Sciences, 1209–1212.

Sekelsky, S. M., and R. E. McIntosh, 1996: Cloud observations with a polarimetric 33 GHz and 95 GHz radar. *Meteor. Atmos. Phys.,* **58,** 123–140.

——, W. L. Ecklund, J. M. Firda, K. S. Gage, and R. E. McIntosh, 1999: Particle size estimation in ice-phase clouds using multifrequency radar reflectivity measurements at 95, 33, and 2.8 GHz. *J. Appl. Meteor.,* **38,** 5–28.

Stephens, G. L., S.-C. Tsay, P. W. Stackhouse, and P. J. Flatau, 1990: The relevance of the microphysical and radiative properties of cirrus clouds to climate and climatic feedback. *J. Atmos. Sci.,* **47,** 1472–1753.

Takano, Y., and K. N. Liou, 1995: Radiative transfer in cirrus clouds. Part III: Light scattering by irregular ice crystals. *J. Atmos. Sci.,* **52,** 818–837.

Yang, P., and K. N. Liou, 1996: Finite-difference time domain method for light scattering by small ice crystals in three-dimensional space. *J. Opt. Soc. Amer.,* **13,** 2072–2085.

Young, S. A., 1995: Analysis of lidar backscatter profiles in optically thin clouds. *Appl. Opt.,* **34,** 7019–7031.

——, C. M. R. Platt, R. T. Austin, and G. R. Patterson, 2000: Optical properties and phase of some midlatitude, midlevel clouds in ECLIPS. *J. Appl. Meteor.,* **39,** 135–153.